Inhibition mechanisms of AcrF9, AcrF8, and AcrF6 against type I-F CRISPR–Cas complex revealed by cryo-EM

Kaiming Zhang[a,1], Shuo Wang[b,1], Shanshan Li[a,1], Yuwei Zhu[b,1], Grigore D. Pintilie[a], Tung-Chung Mou[c], Michael F. Schmid[d], Zhiwei Huang[b,2], and Wah Chiu[a,d,2]

[a]Department of Bioengineering, James H. Clark Center, Stanford University, Stanford, CA 94305; [b]Harbin Institute of Technology (HIT) Center for Life Sciences, School of Life Science and Technology, Harbin Institute of Technology, 150080 Harbin, China; [c]Center for Biomolecular Structure and Dynamics, University of Montana, Missoula, MT 59812; and [d]CryoEM and Bioimaging Division, Stanford Synchrotron Radiation Lightsource (SSRL), Stanford Linear Accelerator Center (SLAC) National Accelerator Laboratory, Stanford University, Menlo Park, CA 94025

Contributed by Wah Chiu, February 7, 2020 (sent for review December 27, 2019; reviewed by Irina Gutsche and Jinbiao Ma)

Prokaryotes and viruses have fought a long battle against each other. Prokaryotes use CRISPR–Cas-mediated adaptive immunity, while conversely, viruses evolve multiple anti-CRISPR (Acr) proteins to defeat these CRISPR–Cas systems. The type I-F CRISPR–Cas system in *Pseudomonas aeruginosa* requires the crRNA-guided surveillance complex (Csy complex) to recognize the invading DNA. Although some Acr proteins against the Csy complex have been reported, other relevant Acr proteins still need studies to understand their mechanisms. Here, we obtain three structures of previously unresolved Acr proteins (AcrF9, AcrF8, and AcrF6) bound to the Csy complex using electron cryo-microscopy (cryo-EM), with resolution at 2.57 Å, 3.42 Å, and 3.15 Å, respectively. The 2.57-Å structure reveals fine details for each molecular component within the Csy complex as well as the direct and water-mediated interactions between proteins and CRISPR RNA (crRNA). Our structures also show unambiguously how these Acr proteins bind differently to the Csy complex. AcrF9 binds to key DNA-binding sites on the Csy spiral backbone. AcrF6 binds at the junction between Cas7.6f and Cas8f, which is critical for DNA duplex splitting. AcrF8 binds to a distinct position on the Csy spiral backbone and forms interactions with crRNA, which has not been seen in other Acr proteins against the Csy complex. Our structure-guided mutagenesis and biochemistry experiments further support the anti-CRISPR mechanisms of these Acr proteins. Our findings support the convergent consequence of inhibiting degradation of invading DNA by these Acr proteins, albeit with different modes of interactions with the type I-F CRISPR–Cas system.

CRISPR-Csy | anti-CRISPR | cryo-EM

The war between prokaryotes and viruses has been going on for millions of years. Prokaryotes utilize the adaptive immune systems composed of CRISPR (clustered regularly interspaced short palindromic repeats) and CRISPR-associated (Cas) genes to combat viruses (1). The assembly of CRISPR–Cas complex requires one or multiple Cas proteins and a small CRISPR RNA (crRNA), targeting and destroying the invading DNA and/or RNA with a sequence complementary to crRNA. CRISPR–Cas complexes are allocated to two classes, including multi-Cas types I, III, and IV in class I, and single-Cas types II, V, and VI in class II. The type I CRISPR–Cas systems are further divided into seven subtypes, including I-F (2). The type I-F system requires a crRNA-guided surveillance complex (Csy complex) to recognize foreign DNA and recruit a nuclease-helicase protein (i.e., Cas2/3) for DNA degradation (3). The Csy complex is comprised of four types of Cas proteins (Cas5f-8f) and a single 60-nt crRNA, with a stoichiometry of $Cas5f_1 6f_1 7f_6 8f_1$:$crRNA_1$ (4).

In return, the viruses evolve various anti-CRISPR (Acr) proteins to recognize and neutralize the CRISPR–Cas systems. About 22 families of Acr genes have been identified. Due to their low sequence similarity, the Acr genes were classified according to the targeted CRISPR–Cas complexes, including class I and class II Acr proteins (5). To understand how the Acr proteins antagonize the CRISPR–Cas systems, researchers focused on studying the structures of the Acr proteins with or without the targeted CRISPR–Cas complexes. Until now, the structures of more than 10 Acr proteins have been determined (6–9), which either inhibit DNA binding or prevent DNA cleavage by CRISPR–Cas complexes. AcrF9, AcrF8, and AcrF6 were first discovered in 2016 by a bioinformatics method (10); however, their structures and mechanisms of anti-CRISPR activities have not yet been resolved.

In this study, we performed electron cryo-microscopy (cryo-EM) to determine the structures of AcrF9, AcrF8, or AcrF6 bound to their target, the Csy complex from *Pseudomonas aeruginosa*. The resulting maps were well resolved, especially for the Csy complex bound with AcrF9, with an overall resolution of 2.57 Å. These high-resolution structures enabled de novo model building and uncovered the intermolecular interactions between these Acr proteins and the Csy complex. Further mutagenesis experiments guided by our structures showed that AcrF9, AcrF8,

Significance

CRISPR–Cas systems are widely distributed adaptive immune systems in prokaryotes that protect against invading genetic materials. To survive inside the prokaryotic host cells, viruses have developed various strategies to compromise the CRISPR–Cas systems, including the anti-CRISPR (Acr) proteins. Here, we report three atomic models of AcrF9, AcrF8, and AcrF6, each of which is found to bind to the type I-F CRISPR–Cas system differently using cryo-EM. These structures guide mutagenesis and biochemical experiments to derive their mechanisms to produce anti-CRISPR activities. Our data show their diverse modes of interactions but yield the same effect in barring the degradation of the viral DNA.

Author contributions: K.Z. and Z.H. designed research; K.Z., S.W., S.L., Y.Z., G.D.P., and T.-C.M. performed research; K.Z.,S.L., G.D.P., M.F.S., Z.H., and W.C. analyzed data; and K.Z., S.L., and W.C. wrote the paper.

Reviewers: I.G., Institut de Biologie Structurale; and J.M., Fudan University.

The authors declare no competing interest.

This open access article is distributed under Creative Commons Attribution-NonCommercial-NoDerivatives License 4.0 (CC BY-NC-ND).

Data deposition: The atomic coordinates and structure factors have been deposited in the Electron Microscopy Data Bank (EMD), https://www.ebi.ac.uk/pdbe/emdb (accession codes EMD-21358–EMD-21360) and the Protein Data Bank, www.wwpdb.org (PDB ID codes 6VQV–6VQX).

[1]K.Z., S.W., S.L., and Y.Z. contributed equally to this work.

[2]To whom correspondence may be addressed. Email: huangzhiwei@hit.edu.cn or wahc@stanford.edu.

This article contains supporting information online at https://www.pnas.org/lookup/suppl/doi:10.1073/pnas.1922638117/-/DCSupplemental.

First published March 13, 2020.

Downloaded by guest on October 28, 2020

and AcrF6 bind different sites on the Csy complex to prevent the target DNA from binding to the complex. Our study provides the most detailed insight into the molecular basis of blocking the type I-F CRISPR–Cas system and expands the library of the structures and mechanisms of action of the Acr proteins.

Results

Overall Cryo-EM Structures of the Csy Complex. Using cryo-EM single-particle analysis, we obtained the structures of Csy complex bound with its inhibitors: AcrF9, AcrF8, or AcrF6, with the overall resolution of 2.57 Å, 3.42 Å, or 3.15 Å, respectively. Cryo-EM micrographs, two-dimensional (2D) class averages, and final three-dimensional (3D) reconstructions of the Csy complexes display a "G" shape (*SI Appendix*, Figs. S1–S4). Similarly to other Csy–Acr complexes (11–14), the maps exhibit an asymmetric spiral, with one Cas6f subunit in the head, one Cas5f and one Cas8f in the tail, and six Cas7f comprising the spiral backbone (Fig. 1). The Acr proteins either bind to the Cas7f backbone (AcrF9, AcrF8) or insert between the Cas7f and Cas8f subunits in the tail region (AcrF6) (Fig. 1).

The map quality is sufficient for the de novo model building of the three Acr proteins into their respective complexes. The quality of these models was validated by MolProbity (15) (*SI Appendix*, Table S1). The Q-scores (16) developed for evaluating the density resolvability were used to assess the quality of these cryo-EM structures (*SI Appendix*, Figs. S5 and S6).

To obtain the most detailed organizational principle of Csy complex assembly, we analyzed the intermolecular interactions within the model derived from the 2.57-Å cryo-EM map (*SI Appendix*, Fig. S7 and Movie S1). The six copies of the hand-shaped backbone protein Cas7 are arranged in the same direction along the spiral, creating five equivalent interfaces between them. They share the same conformation, as demonstrated by the rmsd of less than 0.7 Å for equivalently positioned Cα atoms (*SI Appendix*, Fig. S7*C*). We illustrate the interactions between Cas7f subunits by the example of Cas7.4f and Cas7.5f. The thumb of Cas7.5f traverses the palm of Cas7.4f, and the interface area between them was about 2,000 $Å^2$, involving extensive salt bridges and hydrogen bonds (*SI Appendix*, Fig. S7*D* and Table S2). The thumbs of the

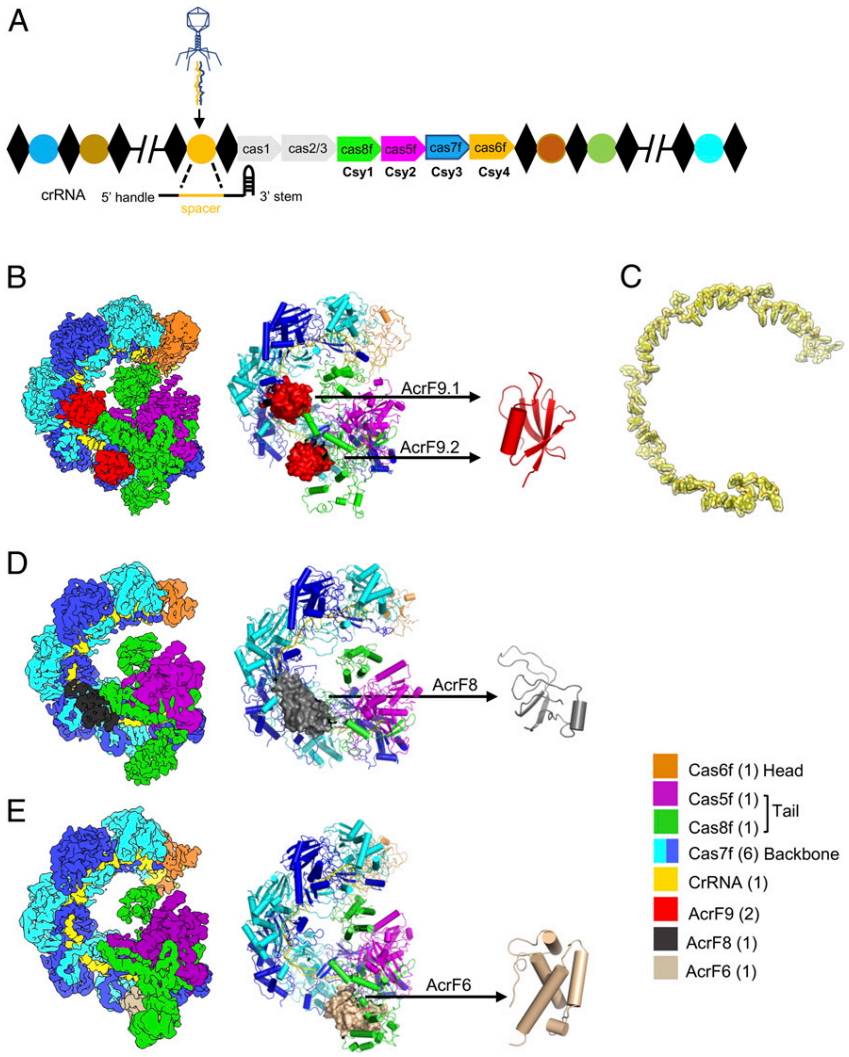

Fig. 1. Overall structures of Csy–Acr complexes. (*A*) Schematic representation of the CRISPR loci separated by *cas* genes in the host genome. The CRISPR loci includes multiple direct repeats (black diamonds) that are separated by virus-derived spacer sequences (spheres in different colors). (*B*) The 2.57-Å cryo-EM map and model of the Csy complex bound with AcrF9 (red). (*C*) Individual density and model of the crRNA (residues 1–40) derived from *B*. (*D*) The 3.42-Å cryo-EM map and model of the Csy complex bound with AcrF8 (gray). (*E*) The 3.15-Å cryo-EM map and model of the Csy complex bound with AcrF6 (tan). The Csy complex in *B*, *D*, and *E* consists of nine Cas proteins and one crRNA, shown in distinct colors.

Downloaded by guest on October 28, 2020

spiral backbone proteins (Cas7f) distort the crRNA at 6-nt intervals, similar to what has been reported in other type I and type III CRISPR–Cas systems (17–19). Cas7f and crRNA form multiple hydrogen bonds, which mostly occur between the arginine-rich region (F32, R34, R68, Q95, R168, Q247, Q276, K277, R283, S308, R350) and the sugar-phosphate backbone of crRNA, with only two nucleobases (G[+14], G[+19]) involved (*SI Appendix*, Fig. S7*E*). This finding indicates the nonsequence-specific crRNA recognition mode of Cas7f. In addition, we observed water-mediated interactions between Cas7f and crRNA via nucleobases, which were also confirmed in two half-maps (*SI Appendix*, Fig. S7*F*). Structure-based sequence alignment shows that in different species, the Cas7f protein residues involved in crRNA interactions are highly conserved, indicating the existence of a conserved crRNA recognition mechanism in Cas7f (*SI Appendix*, Fig. S8). Furthermore, the Cas5f and Cas8f subunits in the tail region also make extensive interactions with crRNA, causing the 8 nt of crRNA at its 5′ terminus to display an "S"-shape architecture, called the 5′ handle (*SI Appendix*, Fig. S9). It is noteworthy, however, that the majority of interactions occur on the nucleobases of this 5′ handle, supporting a sequence-specific recognition of the crRNA 5′ handle by Cas5f and Cas8f, consistent with previous biochemical findings (20).

AcrF9 Proteins Bind to the Csy Spiral Backbone to Prevent DNA Binding. As shown in Figs. 1*B* and 2*A*, the 68-residue AcrF9 is composed of a pair of antiparallel β-sheets separated by a single α-helix ($\beta_1\beta_2\alpha_1\beta_3\beta_4$), and two copies bind to a single Csy complex. Each of AcrF9 sits between the thumb and loop regions of Cas7.4f and Cas7.6f, respectively. Analysis of the surface electrostatic potential showed that positively charged residues on the thumb region (K76, K78, K84) and loop region (K253, K256/7, K260, K262) of Cas7f generate a vise-like structure (Fig. 2*B*). We propose that AcrF9 docks into this vise via electrostatic interaction, which is further stabilized by other types of interactions.

To understand how AcrF9 suppresses the Csy complex, we analyzed our observed interactions between AcrF9 and Csy complex using PDBsum (21), with multiple hydrogen bonds (e.g., $Q38_{AcrF9}$:$K78_{Cas7f}$) and hydrophobic interactions (e.g., $F40_{AcrF9}$:$R74_{Cas7f}$ and $F40_{AcrF9}$:$K76_{Cas7f}$) found (Fig. 2 *C* and *D* and *SI Appendix*, Fig. S10). Notably, a lysine-rich region of the Cas7f subunit (K76, K78, K84, and K256) has been reported to be critical for DNA binding by the Csy complex (13), and it also interacts extensively with AcrF9 (Fig. 2 *C* and *D*), suggesting that AcrF9 may competitively bind to DNA binding sites of the Csy complex. We thus made mutations on AcrF9 (Q38A and F40A), which were designed to interrupt their respective interactions with K78 and K76 of Cas7f. We then performed in vitro cleavage activity assays in the presence of Csy complex and Cas3 to explore whether these mutations rescue the DNA cleavage activity of Csy–Cas3 complex. WT AcrF9 inhibits the DNA binding and subsequent Cas3 recruitment of the Csy complex, suppressing DNA degradation. In contrast, the AcrF9 mutants abolish the

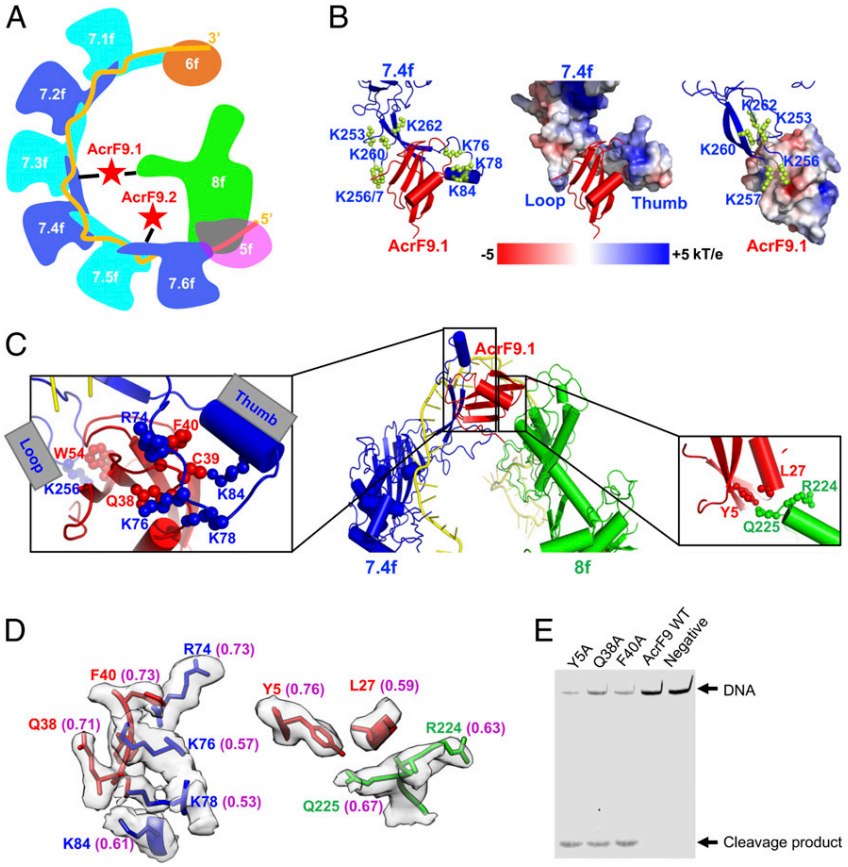

Fig. 2. Anti-CRISPR protein AcrF9 binds to key DNA-binding sites on the Csy complex. (*A*) The cartoon shows the architecture of the Csy complex bound with two copies of AcrF9. Interacting domain between Cas7.4f and AcrF9 (*B*, *Left*); electrostatic representation of Cas7.4f in a lysine-rich region (*B*, *Center*); electrostatic representation of AcrF9 (*B*, *Right*). (*C*) Interactions of AcrF9.1 with Cas7.4f and Cas8f. The interacting residues are shown in sphere. (*D*) Zoom-in map and model view of the interacting region between AcrF9.1 and Cas7.4f, as well as AcrF9.1 and Cas8f with Q-scores annotated (magenta), demonstrating the good resolvability of involved amino acid residues. (*E*) Mutations of the residues on ArcF9 interacting with Cas7.4f and Cas8f impaired the anti-CRISPR function of ArcF9. The negative control represents Csy complex plus labeled DNA without Cas3.

Downloaded by guest on October 28, 2020

inhibition of AcrF9 on the above processes, and the substrate DNA is rapidly degraded (Fig. 2*E*), supporting the notion that AcrF9 exerts its anti-CRISPR function via competitively binding to DNA binding sites (e.g., K76 and K78) on the Cas7f subunits of the Csy complex.

AcrF9.1 also contacts with Cas8f. The interface area between them is about 240 Å^2 and involves two hydrogen bonds (Y5:Q225 and L27:R224) (Fig. 2 *C* and *D*). This interaction leads to an overall conformational change that causes the loop region (S223-S227) of Cas8f to move into the closed position, locking the complex with AcrF9 (*SI Appendix*, Fig. S11*A*). AcrF9 mutant (Y5A) that is designed to interrupt its interaction with Q225 of Cas8f also disrupts the anti-CRISPR function of AcrF9 (Fig. 2*E*). Interestingly, a structural homology search of AcrF9 using DALI (22) revealed Cas2 and Cas3 (CRISPR-associated proteins) as the top hits, with an rmsd of 1.5 Å and 1.163 Å, respectively (*SI Appendix*, Fig. S11*B*). The Cas3 protein (*P. aeruginosa*) was proposed to interact with the C-terminal helical bundle of Cas8f (11). Further biochemical and structure experiments are needed to elucidate whether AcrF9 also inhibits Cas2/3-mediated DNA degradation by competing for the same binding domains on Cas8f.

AcrF8 Binds to the Csy Spiral Backbone to Prevent DNA Hybridization. AcrF8 is a 92-residue protein, with a single copy occupying the cavity surrounded by Cas5f, Cas7.4–7.6f, and Cas8f (Figs. 1*D* and 3*A*). By using PDBsum (21) that analyzes and predicts interactions, a positively charged residue-rich region generated by Cas5f (K76), Cas7.6f (K257), and Cas8f (R210, K216) forms multiple nonbonded contacts with the α-helix of AcrF8 (Fig. 3*B*), which may be important for AcrF8 docking into the Csy complex. The distance between the residues T29, I31, A32, N33 of AcrF8 and the nucleobases of three nucleotides (U[+21], U[+22], G[+23]) of crRNA is less than 4 Å, which is close enough to form multiple hydrogen bonds and nonbonded interactions (Fig. 3 *B* and *C*). Besides, the above three nucleotides are located just after the kink caused by the thumb of Cas7.5f, whose interactions with AcrF8 thereby form a continuous 4-nt region that would interfere with the DNA-crRNA hybridization and subsequent DNA degradation. To test this hypothesis, we recombinantly expressed the AcrF8 containing a mutation at position 31 (I31A) or position 32 (A32G), which leads to an increase in the cleavage of DNA substrate compared with the WT AcrF8 (Fig. 3*D*); this finding indicates that AcrF8 perturbs DNA substrate hybridization and degradation. Besides, we also observed interactions between Cas7.5f (L94, K260) and AcrF8 (T43), with distances less than 2.7 Å, which might contribute to the stabilization of the AcrF8-crRNA hybrid (Fig. 3*B*).

AcrF6 Binds at the Junction between Cas7.6f and Cas8f to Inhibit DNA Duplex Splitting. The 100-residue AcrF6 is an α-helix–only structure, differing from AcrF8 and AcrF9 that are comprised of α-helices and β-sheets (Fig. 1*E* and *SI Appendix*, Fig. S12). It localizes to the tail region of the Csy complex and has close interactions with Cas8f, Cas7.6f, and Cas5f (Fig. 4*A*). Positively charged residues on Cas7.6f (R74, K76, K78) and Cas5f (R85) form extensive nonbonded contacts with AcrF6, which may play a role in the docking of AcrF6 into the Csy complex. The interface area between AcrF6 and Cas8f occupies about 700 Å^2 and involves two salt bridges (D41:K247, D45:K247) and one hydrogen bond (Y38:T246) (Fig. 4 *B* and *C*). Residue K247 of Cas8f has been shown to promote foreign DNA duplex splitting by wedging into the strands, which is a prerequisite for DNA binding to Csy (11). Therefore, AcrF6 may interfere with DNA duplex splitting and subsequent DNA-crRNA hybridization to inhibit its degradation. To confirm the residue candidates that are important for the anti-CRISPR function of AcrF6, we introduced multiple mutations into the AcrF6 subunit (Y38A, Y38W, D41A, or D45A) and measured their effects on the cleavage of DNA substrate by the Csy–Cas3 complex. We found that these mutations result in much stronger DNA cleavage activities of Cas3 compared to the WT AcrF6 (Fig. 4*D*). Moreover, a hydrogen bond is formed between the N10 of AcrF6 and the U[+10] of crRNA, and a double mutation at positions 10 and 38 (N10A/Y38A) further enhances the DNA cleavage activity of Cas3 compared with the Y38A mutant (Fig. 4 *B* and *D*). Therefore, these findings suggest that AcrF6 inhibits the Csy complex by targeting the DNA duplex splitting and binding.

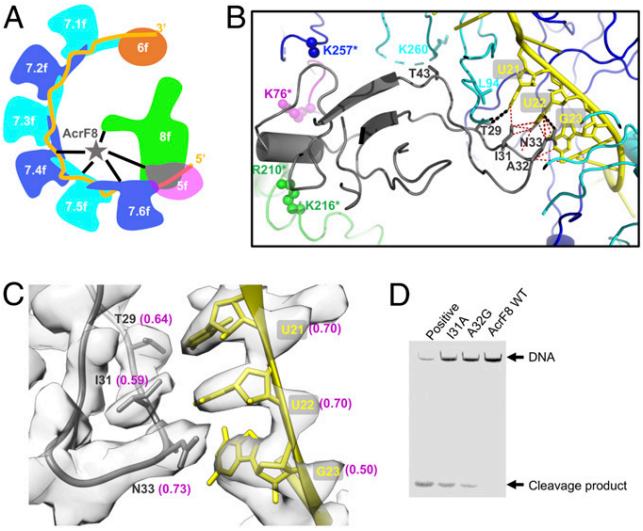

Fig. 3. AcrF8 binds to the Csy spiral backbone to prevent DNA hybridization. (*A*) The cartoon shows the architecture of the Csy complex bound with one copy of AcrF8. (*B*) Interactions of AcrF8 with multiple components of the Csy complex including crRNA. The nonbonded contacts between AcrF8 and crRNA are shown in red dash lines, while the hydrogen bonds are shown in black dash lines. (*C*) Zoom-in map and model view of the interacting region between AcrF8 and crRNA with Q-scores annotated (magenta), demonstrating the good resolvability of involved amino acid residues and nucleobases. (*D*) Mutations of the residues on ArcF8 interacting with crRNA impaired the anti-CRISPR function of ArcF8. The positive control represents Cas3 cleavage of the labeled DNA without AcrF8.

Discussion

Our near-atomic resolution cryo-EM structures allowed us to confidently build atomic models of three Acr proteins. A comparison of all Acr proteins with known structures shows that they share some structural similarities despite low sequence identity. AcrF1, AcrF2 (12, 13), AcrF8, AcrF9, AcrF10 (12), and AcrIIA4 (23) all exhibit the α/β-fold, namely, β-sheets with variable numbers of α-helices positioned along one or both sides (*SI Appendix*, Fig. S12). Besides, they employ a similar inhibitory mechanism to block invading DNA recognition, with the big difference being in their binding sites. It is worth noting that the binding sites of these Acr proteins are mainly localized in their β-sheets and loop regions (Figs. 2*C* and 3*B*). The α-helix might enclose a hydrophobic surface to promote the stabilization of protein structures. Like AcrF3 (24, 25), AcrIIA1 (26), and AcrVA1 (8), AcrF6 is formed exclusively of α-helices (*SI Appendix*, Fig. S12). However, their mechanisms of action vary greatly. Both AcrF3 and AcrVA1 assemble into a dimer, but AcrF3 binds Cas3 to block its recruitment by the Csy complex, while AcrVA1 binds Cas12a to cleave crRNA to render Cas12a inactive. The inhibitory mechanism of dimerized AcrIIA1 is still unknown; however, it has been reported to be copurified with RNA, suggesting its direct effect on nucleotides. Our results suggest that AcrF6 monomer, not a dimer, blocks DNA access to

Downloaded by guest on October 28, 2020

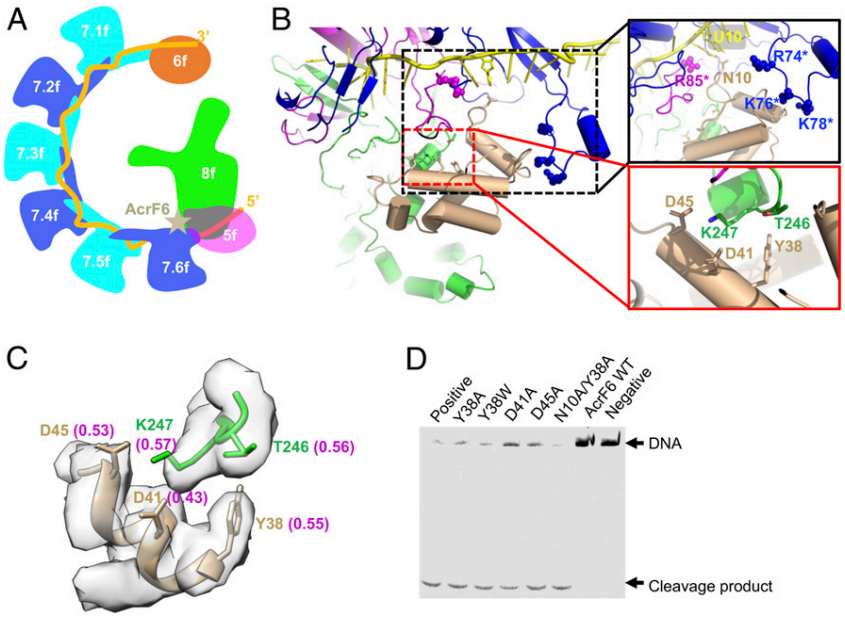

Fig. 4. AcrF6 binds at the junction between Cas7.6f and Cas8f to inhibit DNA duplex splitting. (*A*) The cartoon shows the architecture of the Csy complex bound with one copy of AcrF6. (*B*) Interactions of AcrF6 with multiple components (Cas5f, Cas7.6f, Cas8f, and crRNA) of the Csy complex. (*C*) Zoom-in map and model view of the interacting region between AcrF6 and Cas8f with Q-scores annotated (magenta), demonstrating the good resolvability of involved amino acid residues. (*D*) Mutations of the residues on ArcF6 interacting with Cas8f and crRNA impaired the anti-CRISPR function of ArcF6. The positive control represents Cas3 cleavage of the labeled DNA without AcrF6 and the negative control represents Csy complex plus labeled DNA without Cas3.

its binding site. Therefore, it is difficult to judge the mechanism of action based solely on structural information of Acr proteins.

Previous research has shown that a single type of Acr protein is sufficient to silence the Csy function (27). However, various Acr proteins were discovered to suppress the activity of the Csy complex by preferentially binding to certain regions on the Csy complex. Like AcrF2 and AcrF10, AcrF6 also binds in the junction region between Cas 7.6f and Cas8f subunits of the Csy complex to compete for foreign DNA binding (Fig. 5). It is worth discussing why multiple Acr proteins act on a similar region. In nature, no species can unlimitedly duplicate, and there must be a balance between them (5). It is therefore tempting to speculate that the prokaryotes evolve new measures to inactivate the anti-CRISPR activity, such as anti-Acr proteins (6). The existence of anti-anti-CRISPR activity might explain the redundancy of Acr proteins. For Acr proteins located between Cas7.6f-Cas8 (e.g., AcrF2) (Fig. 5), a single copy can inhibit the Csy complex-mediated target DNA recognition. However, for the Acr protein bound to the Cas7f spiral backbone (e.g., AcrF1) (Fig. 5), the number of copies required for DNA binding inhibition remains unknown, depending on the extent to which it blocks the spacer sequence (14). Based on these findings, one copy of AcrF6 should be able to effectively prevent the DNA binding while the copy numbers of AcrF8 and AcrF9 required to attain the goal of inhibition need further study.

Although multiple Acr proteins have been demonstrated as DNA mimics (8, 12, 13, 23, 28, 29), our study unprecedentedly shows that direct interactions between Acr proteins (AcrF8 and

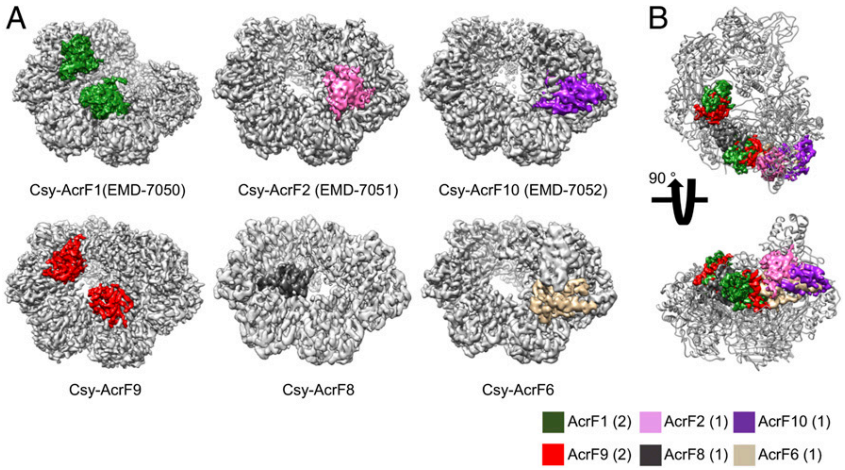

Fig. 5. Acr proteins bind to the Csy complex with different copies and preferred binding sites. (*A*) Cryo-EM maps of Csy–Acr complexes from previous studies and this work, with Acr proteins highlighted in different colors. (*B*) Acr proteins preferentially bind to the lower half body of the Csy complex.

Downloaded by guest on October 28, 2020

AcrF6) and crRNA are required for the inhibition by Acr proteins, especially for AcrF8. Notably, the crRNA moieties recognized by AcrF8 and AcrF6 are nucleobases (Figs. 3*B* and 4*B*), supporting the idea that AcrF8 and AcrF6 bind to the crRNA in a sequence-dependent manner, to some extent similar to target DNA.

The CRISPR–Cas-mediated adaptive immune response can be divided into three steps, including the acquisition of spacer derived from invading nucleic acids, crRNA processing, and target degradation (30). Theoretically, Acr proteins could suppress any phase to disrupt the CRISPR–Cas system. However, our study combined with previous reports reveal that the Acr proteins mainly target the third step. The other Acr genes deserve further research to explore if other new mechanisms exist, such as encoding Cas protein or crRNA mimics to disrupt the assembly of the CRISPR–Cas systems.

Materials and Methods

Protein Expression and Purification. The plasmids pCsy_complex (#89232) and pCRISPR_DMS3g24 (#89244) were purchased from Addgene (3, 4). *Escherichia coli* C43 (DE3) cells were transformed with these two plasmids and cultured at 37 °C. Isopropyl-β-D-thiogalactoside (IPTG; 0.3 mM) was added to induce the expression of the Csy complex for about ∼12 h. The cells were obtained by centrifugation at 23,708 × *g* and placed in a buffer containing 25 mM Tris·HCl (pH 8.0), 150 mM NaCl, 5% glycerol, and 1 mM phenylmethanesulfonyl fluoride (PMSF). The cells were lysed ultrasonically and centrifuged to remove the precipitate. The supernatant containing proteins was purified with the Ni^{2+}-NTA agarose. After washing, a buffer containing 25 mM Tris·HCl (pH 8.0), 150 mM NaCl, 300 mM imidazole, and 10% glycerol was used to elute proteins bound to agarose. The resultant protein solution was further purified by fast protein liquid chromatography (FPLC; GE Healthcare).

Cas3 and AcrF6/8/9 (WT or mutant) genes were cloned into pGEX-6P-1 with an N-terminal GST tag (GE Healthcare). DE3 cells were transformed with these plasmids and cultured at 37 °C. After IPTG induction, the cells were collected in a buffer containing 25 mM Tris·HCl (pH 8.0), 500 mM NaCl, 3 mM dithiothreitol (DTT), and 1 mM PMSF. The cells were then lysed, and the lysates were purified with glutathione Sepharose 4B (GS4B) beads (GE Healthcare). After washing, the proteins bound to GS4B beads were released by preScission protease cleavage. The Cas3 protein was further purified by FPLC, while the AcrF6/8/9 were fractionated by ion-exchange chromatography or concentrated to use after elution.

For the purification of the Csy complex bound with its inhibitor AcrF9, AcrF8, or AcrF6, the Csy complex was incubated with the individual Acr protein at different ratios (Csy complex:AcrF6 = 1:15, Csy complex:AcrF8 = 1:6, Csy complex:AcrF9 = 1:20). Then the complexes were separated by size-exclusion chromatography (GE Healthcare) with a buffer containing 20 mM Hepes (pH 7.5), 100 mM KCl, and 1 mM Tris(2-carboxyethyl)phosphine hydrochloride (TCEP). Purified proteins were finally flash-frozen in liquid nitrogen.

Cryo-EM Data Acquisition. The samples were diluted at a final concentration of around 0.4 mg/mL for Csy–AcrF6 complex, and 0.15 mg/mL for Csy–AcrF8 and Csy–AcrF9 complexes. Three microliters of the samples were applied onto glow-discharged 200-mesh R2/1 Quantifoil grids. The grids were blotted for 2–4 s and rapidly cryocooled in liquid ethane using a Vitrobot Mark IV (Thermo Fisher Scientific) at 4 °C and 100% humidity. Notably, at the initial screening using a Talos Arctica cryo-electron microscope (Thermo Fisher Scientific) operated at 200 kV, the preferred orientation was very severe for the Csy–AcrF8 and Csy–AcrF9 complexes. To avoid this issue, the grids for Csy–AcrF8 and Csy–AcrF9 complexes were coated by thin continuous carbon treated with 2% (wt/vol) poly-lysine. The samples were then imaged in a Titan Krios cryo-electron microscope (Thermo Fisher Scientific) with GIF energy filter (Gatan) at a magnification of 130,000× (corresponding to a calibrated sampling of 1.06 Å per pixel) for Csy–AcrF6 and Csy–AcrF8, and at a magnification of 215,000× (corresponding to a calibrated sampling of 0.65 Å per pixel) for Csy–AcrF9. Micrographs were recorded by EPU software (Thermo Fisher Scientific) with a Gatan K2 Summit direct electron detector, where each image was composed of 30 individual frames with an exposure time of 6 s and an exposure rate of 7.6 electrons per second per $Å^2$ for Csy–AcrF6 and Csy–AcrF8, and 7 electrons per second per $Å^2$ for Csy–AcrF9. A total of 1,956 movie stacks for Csy–AcrF6, 6,338 movie stacks for Csy–AcrF8, and 9,267 movie stacks for Csy–AcrF9 were collected.

Single-Particle Image Processing and 3D Reconstruction. All micrographs were imported into Relion (31) for image processing and 3D reconstruction. The motion correction was performed using MotionCor2 (32) and the contrast transfer function (CTF) was determined using CTFFIND4 (33). Then the micrographs with "rlnMotionEarly < 10" and "rlnCtfMaxResolution < 5" were selected using "subset selection" option in Relion. All particles were auto-picked using NeuralNet option (threshold 1 = 0; threshold 2 = −5) in EMAN2 (34), and further checked manually. Then, particle coordinates were imported to Relion, where the 2D/3D classification and 3D refinement were performed. The poor 2D class averages were then removed by 2D classification for couple rounds of refinement (three rounds for Csy–AcrF9, Csy–AcrF8 and four rounds for Csy–AcrF6; 30 iterations per round). For Csy–AcrF9, a dataset of 595,828 particles was used for 3D classification using the apo-Csy complex map (EMD-7049) as the initial reference model. After two rounds of 3D classification, the bad classes with ∼260,000 particles were removed. Next, the final 3D refinement was performed using 332,404 particles, and a 2.57-Å map was achieved. For Csy–AcrF8, a total of 288,565 particles was used for 3D classification. After one round of 3D classification, one bad class with 29.4% of the particle images was removed. Next, 3D refinement was performed using 203,438 particles, with a 3.5-Å map obtained. In order to achieve a better quality of AcrF8 density, another round of 3D classification without alignment was performed, and two classes with the poor density of AcrF8 were removed. Final 3D refinement was performed using 91,080 particles, and a 3.42-Å map was achieved. For Csy–AcrF6, a total dataset of 301,900 particles was used for three rounds of 3D classification to remove the bad classes. The final 3D refinement was performed using 56,455 particles, with a 3.15-Å map obtained (see more information in *SI Appendix*, Figs. S2–S4 and Table S1). For all maps, we used the default parameters in Relion for sharpening.

Docking and de Novo Model Building. The unbound Csy complex (PDB ID code 6B45) was first used for docking into the 2.57-Å cryo-EM map of Csy complex bound with AcrF9. Then two unmodeled cryo-EM density regions, possibly derived from AcrF9, were found, with one of which being computationally extracted from our map (35). Based on the extracted cryo-EM map, the de novo model building of AcrF9 was performed using Coot (36). Amino acid sequence registration was assigned initially to the cryo-EM density of bulky residues (Trp, Lys, Arg, Phe, and Tyr) and then to the rest of the residues. The resulting model was refined using phenix.real_space_refine (37) application with secondary structure and geometry restraints. Coot was used to manually optimize the model. After the full-length AcrF9 was modeled, the whole Csy-ArcF9 model was optimized by using phenix.real_space_refine.

The same procedures were performed for the model building of AcrF6 or AcrF8 protein bound to the Csy complex, with 97 of 100 residues or 80 of 92 residues being modeled, respectively.

The final models of Csy-AcrF complexes were evaluated as previously described (38), including MolProbity (15) and Q-scores (16). Statistics of the map reconstruction and model optimization are shown in *SI Appendix*, Table S1. PDBsum structure bioinformatics software (21) was used to analyze our structure models to identify the key residues involved in interactions between different subunits. All figures were prepared using PyMol (39), Chimera (40), and ChimeraX (41).

Cleavage Activity Assays. Cleavage assays were performed in the 15-μL reaction buffer (25 mM Hepes, pH 7.5, 60 mM KCl, 5% Glycerol, 2 mM $MgCl_2$, 2 mM Adenosine triphosphate (ATP), 10 μM $CoCl_2$) containing 1 μM Csy complex, proper amount of AcrF6/8/9, 0.7 μM Cas3, and 50 ng of double-strand DNA (dsDNA) labeled by maleimide at the 5′-end. The ratios of Csy complex and AcrF6/8/9 are shown as follows: Csy complex:AcrF6 = 1:1, Csy complex:AcrF8 = 1:20, Csy complex:AcrF9 = 1:4. The Csy complex and the AcrF6/8/9 variants were first incubated for 5 min, followed by the addition of Cas3 and DNA substrate. Cleavage reactions were conducted at 37 °C for 13 min. Reactions were stopped by adding 2× TBE (Tris-Borate-EDTA)-urea loading buffer. Cleavage products were run on 10% TBE-Urea denaturing gel at room temperature in 1× TBE running buffer and visualized by fluorescence imaging. The sequence for the DNA substrate is listed as below, with the complementary segment to crRNA underlined:

TCGGTGCGGGCCTCTTCGCTATTACGCCAGCTGGCGAAAGGGGGATGTGCTG-CAAGGCGATTAAGTTGGGTAACGCCAGGGTTTTCCCAGTCACGACGTTGTAAAAC-GACGGCCAGTGCCAAGCTTGCATGCCTGCAGGTCGACTCTAGAGGATCCGCT-GTACGTCACTATCGAAGCAATACAGGTAGACGCGGACATCAAGCCCGCCG-TGAAGGTGCAGCTTCTCTACAGAGTGCGAATTCGTAATCATGGTCATAGCTG-TTTCCTGTGTGAAAT

Data Deposition. Cryo-EM maps of the Csy–ArcF9, Csy–AcrF8, and Csy–AcrF6 with their associated atomic models have been deposited in the Electron Microscopy Data Bank and the Protein Data Bank under accession codes EMD-21358, EMD-21359, and EMD-21360; and PDB ID codes 6VQV, 6VQW, and 6VQX.

ACKNOWLEDGMENTS. This research is supported by NIH Grants P41GM103832, R01GM079429, and S10OD021600 (to W.C.); National Natural Science Foundation of China Grants 31825008 and 31422014 (to Z.H.), and 31800630 (to Y.Z.); and the Fundamental Research Funds for the Central Universities HIT.NSRIF.2019067 (to Y.Z.).

Downloaded by guest on October 28, 2020

1. R. Barrangou *et al*., CRISPR provides acquired resistance against viruses in prokaryotes. *Science* **315**, 1709–1712 (2007).
2. K. S. Makarova *et al*., An updated evolutionary classification of CRISPR-Cas systems. *Nat. Rev. Microbiol.* **13**, 722–736 (2015).
3. M. F. Rollins *et al*., Cas1 and the Csy complex are opposing regulators of Cas2/3 nuclease activity. *Proc. Natl. Acad. Sci. U.S.A.* **114**, E5113–E5121 (2017).
4. B. Wiedenheft *et al*., RNA-guided complex from a bacterial immune system enhances target recognition through seed sequence interactions. *Proc. Natl. Acad. Sci. U.S.A.* **108**, 10092–10097 (2011).
5. A. Pawluk, A. R. Davidson, K. L. Maxwell, Anti-CRISPR: Discovery, mechanism and function. *Nat. Rev. Microbiol.* **16**, 12–17 (2018).
6. Y. Zhu, F. Zhang, Z. Huang, Structural insights into the inactivation of CRISPR-Cas systems by diverse anti-CRISPR proteins. *BMC Biol.* **16**, 32 (2018).
7. A. P. Hynes *et al*., Widespread anti-CRISPR proteins in virulent bacteriophages inhibit a range of Cas9 proteins. *Nat. Commun.* **9**, 2919 (2018).
8. H. Zhang *et al*., Structural basis for the inhibition of CRISPR-Cas12a by anti-CRISPR proteins. *Cell Host Microbe* **25**, 815–826.e4 (2019).
9. L. Dong *et al*., An anti-CRISPR protein disables type V Cas12a by acetylation. *Nat. Struct. Mol. Biol.* **26**, 308–314 (2019).
10. A. Pawluk *et al*., Inactivation of CRISPR-Cas systems by anti-CRISPR proteins in diverse bacterial species. *Nat. Microbiol.* **1**, 16085 (2016).
11. M. F. Rollins *et al*., Structure reveals a mechanism of CRISPR-RNA-guided nuclease recruitment and anti-CRISPR viral mimicry. *Mol. Cell* **74**, 132–142.e5 (2019).
12. T. W. Guo *et al*., Cryo-EM structures reveal mechanism and inhibition of DNA targeting by a CRISPR-cas surveillance complex. *Cell* **171**, 414–426.e12 (2017).
13. S. Chowdhury *et al*., Structure reveals mechanisms of viral suppressors that intercept a CRISPR RNA-guided surveillance complex. *Cell* **169**, 47–57.e11 (2017).
14. R. Peng *et al*., Alternate binding modes of anti-CRISPR viral suppressors AcrF1/2 to Csy surveillance complex revealed by cryo-EM structures. *Cell Res.* **27**, 853–864 (2017).
15. V. B. Chen *et al*., MolProbity: All-atom structure validation for macromolecular crystallography. *Acta Crystallogr. D Biol. Crystallogr.* **66**, 12–21 (2010).
16. G. Pintilie *et al*., Measurement of atom resolvability in cryo-EM maps with Q-scores. *Nat. Methods* **17**, 328–334 (2020).
17. D. W. Taylor *et al*., Structural biology. Structures of the CRISPR-Cmr complex reveal mode of RNA target positioning. *Science* **348**, 581–585 (2015).
18. H. Zhao *et al*., Crystal structure of the RNA-guided immune surveillance Cascade complex in Escherichia coli. *Nature* **515**, 147–150 (2014).
19. M. Guo *et al*., Coupling of ssRNA cleavage with DNase activity in type III-A CRISPR-Csm revealed by cryo-EM and biochemistry. *Cell Res.* **29**, 305–312 (2019).
20. S. Hong *et al*., CRISPR RNA and anti-CRISPR protein binding to the Csy1-Csy2 heterodimer in the type I-F CRISPR-Cas system. *J. Biol. Chem.* **293**, 9233 (2018).
21. R. A. Laskowski, J. Jabłońska, L. Pravda, R. S. Vařeková, J. M. Thornton, PDBsum: Structural summaries of PDB entries. *Protein Sci.* **27**, 129–134 (2018).
22. L. Holm, L. M. Laakso, Dali server update. *Nucleic Acids Res.* **44**, W351–W355 (2016).
23. D. Dong *et al*., Structural basis of CRISPR-SpyCas9 inhibition by an anti-CRISPR protein. *Nature* **546**, 436–439 (2017).
24. J. Wang *et al*., A CRISPR evolutionary arms race: Structural insights into viral anti-CRISPR/Cas responses. *Cell Res.* **26**, 1165–1168 (2016).
25. X. Wang *et al*., Structural basis of Cas3 inhibition by the bacteriophage protein AcrF3. *Nat. Struct. Mol. Biol.* **23**, 868–870 (2016).
26. D. Ka, S. Y. An, J.-Y. Suh, E. Bae, Crystal structure of an anti-CRISPR protein, AcrIIA1. *Nucleic Acids Res.* **46**, 485–492 (2018).
27. J. Bondy-Denomy *et al*., Multiple mechanisms for CRISPR-Cas inhibition by anti-CRISPR proteins. *Nature* **526**, 136–139 (2015).
28. H. Yang, D. J. Patel, Inhibition mechanism of an anti-CRISPR suppressor AcrIIA4 targeting SpyCas9. *Mol. Cell* **67**, 117–127.e5 (2017).
29. J. Shin *et al*., Disabling Cas9 by an anti-CRISPR DNA mimic. *Sci. Adv.* **3**, e1701620 (2017).
30. F. Hille, E. Charpentier, CRISPR-Cas: Biology, mechanisms and relevance. *Philos. Trans. R. Soc. Lond. B Biol. Sci.* **371**, 20150496 (2016).
31. S. H. W. Scheres, RELION: Implementation of a Bayesian approach to cryo-EM structure determination. *J. Struct. Biol.* **180**, 519–530 (2012).
32. S. Q. Zheng *et al*., MotionCor2: Anisotropic correction of beam-induced motion for improved cryo-electron microscopy. *Nat. Methods* **14**, 331–332 (2017).
33. A. Rohou, N. Grigorieff, CTFFIND4: Fast and accurate defocus estimation from electron micrographs. *J. Struct. Biol.* **192**, 216–221 (2015).
34. G. Tang *et al*., EMAN2: An extensible image processing suite for electron microscopy. *J. Struct. Biol.* **157**, 38–46 (2007).
35. G. D. Pintilie, J. Zhang, T. D. Goddard, W. Chiu, D. C. Gossard, Quantitative analysis of cryo-EM density map segmentation by watershed and scale-space filtering, and fitting of structures by alignment to regions. *J. Struct. Biol.* **170**, 427–438 (2010).
36. P. Emsley, B. Lohkamp, W. G. Scott, K. Cowtan, Features and development of Coot. *Acta Crystallogr. D Biol. Crystallogr.* **66**, 486–501 (2010).
37. P. D. Adams *et al*., PHENIX: A comprehensive Python-based system for macromolecular structure solution. *Acta Crystallogr. D Biol. Crystallogr.* **66**, 213–221 (2010).
38. K. Zhang *et al*., Cryo-EM structures of Helicobacter pylori vacuolating cytotoxin A oligomeric assemblies at near-atomic resolution. *Proc. Natl. Acad. Sci. U.S.A.* **116**, 6800–6805 (2019).
39. R. E. Rigsby, A. B. Parker, Using the PyMOL application to reinforce visual understanding of protein structure. *Biochem. Mol. Biol. Educ.* **44**, 433–437 (2016).
40. E. F. Pettersen *et al*., UCSF Chimera–A visualization system for exploratory research and analysis. *J. Comput. Chem.* **25**, 1605–1612 (2004).
41. T. D. Goddard *et al*., UCSF ChimeraX: Meeting modern challenges in visualization and analysis. *Protein Sci.* **27**, 14–25 (2018).

Downloaded by guest on October 28, 2020